Progenitor, precursor, and evolution of the dusty remnant of the stellar merger M31-LRN-2015

N. Blagorodnova [ORCID],[1]★ V. Karambelkar,[2] S. M. Adams,[2] M. M. Kasliwal [ORCID],[2] C. S. Kochanek,[3,4] S. Dong,[5] H. Campbell,[6] S. Hodgkin,[7] J. E. Jencson,[8] J. Johansson,[9] S. Kozłowski,[10] R. R. Laher,[11] F. Masci,[11] P. Nugent[12] and U. Rebbapragada[13]

[1]*Department of Astrophysics/IMAPP, Radboud University, NL-6525 XZ Nijmegen, The Netherlands*
[2]*Cahill Center for Astrophysics, California Institute of Technology, Pasadena, CA 91125, USA*
[3]*Department of Astronomy, The Ohio State University, 140 W. 18th Ave., Columbus, OH 43210, USA*
[4]*Center for Cosmology and AstroParticle Physics (CCAPP), The Ohio State University, 191 W. Woodruff Ave., Columbus, OH 43210, USA*
[5]*Kavli Institute for Astronomy and Astrophysics, Peking University, Yi He Yuan Road 5, Hai Dan District, Beijing 100871, China*
[6]*Department of Physics, Faculty of Engineering and Physical Sciences, University of Surrey, Guildford, Surrey GU2 7XH, UK*
[7]*Institute of Astronomy, University of Cambridge, Madingley Road, Cambridge CB3 0HA, UK*
[8]*Steward Observatory, University of Arizona, 933 North Cherry Avenue, Tucson, AZ 85721-0065, USA*
[9]*Department of Physics and Astronomy, Division of Astronomy and Space Physics, Uppsala University, Box 516, SE-751 20 Uppsala, Sweden*
[10]*Astronomical Observatory, University of Warsaw, Al. Ujazdowskie 4, PL-00-478 Warszawa, Poland*
[11]*Infrared Processing and Analysis Center, California Institute of Technology, Pasadena, CA 91125, USA*
[12]*Lawrence Berkeley National Laboratory, Berkeley, CA 94720, USA*
[13]*Jet Propulsion Laboratory, California Institute of Technology, Pasadena, CA 91125, USA*

ABSTRACT
M31-LRN-2015 is a likely stellar merger discovered in the Andromeda Galaxy in 2015. We present new optical to mid-infrared photometry and optical spectroscopy for this event. Archival data show that the source started to brighten ∼2 yr before the nova event. During this precursor phase, the source brightened by ∼3 mag. The light curve at 6 and 1.5 months before the main outburst may show periodicity, with periods of 16 ± 0.3 and 28.1 ± 1.4 d, respectively. This complex emission may be explained by runaway mass-loss from the system after the binary undergoes Roche lobe overflow, leading the system to coalesce in tens of orbital periods. While the progenitor spectral energy distribution shows no evidence of pre-existing warm dust in the system, the remnant forms an optically thick dust shell at approximately four months after the outburst peak. The optical depth of the shell increases dramatically after 1.5 yr, suggesting the existence of shocks that enhance the dust formation process. We propose that the merger remnant is likely an inflated giant obscured by a cooling shell of gas with mass $\sim 0.2\,M_\odot$ ejected at the onset of the common envelope phase.

Key words: binaries: close – stars: evolution – dust, extinction – ISM: jets and outflows – transients: novae.

1 INTRODUCTION

Luminous red novae (LRNe) are an observational class of astrophysical transients with peak luminosities in between novae and supernovae (SNe) ($-3 < M_V < -14$ mag), making them members of the 'gap transients' population (Kasliwal 2012; Pastorello & Fraser 2019). This population includes transients of very diverse nature, such as faint core-collapse SNe, Type Ia SN explosions (Bildsten et al. 2007), Ca-rich (strong) transients (Kasliwal et al. 2012), LRNe (Kulkarni et al. 2007), 2008S-like objects (Botticella et al. 2009; Prieto et al. 2009; Thompson et al. 2009), and LBV-like outbursts (Smith et al. 2011), among others. Within the gap category, there is an observational class characterized by strong interaction with a circumstellar medium (CSM), called intermediate luminosity optical/red

transients (ILOT/ILRT). LRNe belong to this group. Observationally, LRN transients quickly evolve towards colder (redder) temperatures, resembling K- or M-type giant stars. Their spectra are characterized by hydrogen emission lines expanding at velocities $\lesssim 1000$ km s^{-1} and a forest of absorption lines for low-ionization elements. At later stages, the progressively cooling photosphere shows the formation of molecules and new dust in the system, which quickly obscures the optical emission (Kamiński & Tylenda 2011; Kamiński et al. 2015).

Since the discovery of the first 'red variable' about 30 yr ago (M31RV; Rich et al. 1989; Mould et al. 1990), LRNe have been sporadically detected both in the Milky Way and in galaxies within ∼30 Mpc (Kulkarni et al. 2007; Smith et al. 2016; Blagorodnova et al. 2017; Mauerhan et al. 2018; Pastorello et al. 2019b). Although their fainter luminosities pose a challenge to their discovery, a few nearby well-studied cases provided a great wealth of information about their origin as violently interacting binary systems. The best

★ E-mail: n.blagorodnova@astro.ru.nl

example to date is V1309 Sco (Mason et al. 2010). Archival data revealed it to be a contact eclipsing binary, whose period decreased exponentially for several years prior to the nova outburst (Tylenda et al. 2011). Other members of this class include the Galactic stellar mergers V838 Mon (Munari et al. 2002), V4332 Sgr (Martini et al. 1999), and OGLE-2002-BLG-360 (Tylenda et al. 2013).

LRNe provide unique observational clues about the final catastrophic stages of binary interaction, specially the termination of the so-called common envelope (CE) phase. This phase can be initiated by the Darwin instability (Darwin 1879). The spin-up of the primary component in an initially tidally locked binary would extract angular momentum from the orbit, drive the orbital decay, and ultimately initiate Roche lobe overflow (RLOF; Rasio 1995). The donor star (typically the primary evolving off of the main-sequence) overfills its Roche lobe and starts unstable mass transfer towards its companion (see Izzard et al. 2012 for a detailed explanation). This process may culminate with both stars orbiting inside a shared non co-rotating layer of gas, called the CE (Paczynski 1976). The less massive component quickly spirals inwards, transferring the angular momentum of the binary to the envelope. At the termination of this phase, part (or all) of the envelope can be ejected, leaving a more compact binary, or a fully coalesced star.

The light curves of LRNe are potentially powered by three different mechanisms: free expansion and release of thermal energy from hot gas created during the dynamical phase of the merger [similar to 'cooling envelope' emission in SNe; recombination of ionized ejecta (Ivanova et al. 2013b), analogous to SNe IIP, and sustained luminosity due to reprocessed shock emission as the dynamical ejecta runs into surrounding layers of pre-existing gas (Metzger & Pejcha 2017)].

Well-studied stellar mergers are powerful probes of the dynamical onset of CE evolution, which is one of the most challenging phases of binary evolution (see Ivanova et al. 2013a for a review). Currently, there are still important questions to be answered. Which progenitor systems undergoing RLOF result in CE events via dynamically unstable mass transfer? What is the role of pre-outburst mass-loss from the system (Pejcha 2014; Pejcha, Metzger & Tomida 2016a,b; MacLeod, Ostriker & Stone 2018a, b; Reichardt et al. 2019; MacLeod & Loeb 2020)? What is the role of jets in the removal of the envelope (Moreno Méndez, López-Cámara & De Colle 2017; Shiber & Soker 2018; Shiber et al. 2019; Lopez-Camara, Moreno Mendez & De Colle 2020)? How dust forms in the expanding ejecta (Lü, Zhu & Podsiadlowski 2013; Iaconi et al. 2020) and what is the role of dust-driven winds in unbinding the loosely bound envelope after its ejection (Glanz & Perets 2018)? Finally, understanding which CE events result in a complete merger and which result in a close binary binary is crucial for gravitational wave science (Dominik et al. 2012; Klencki et al. 2020; Vigna-Gómez et al. 2020)

The rate of transients associated with stellar mergers is high enough (Kochanek, Adams & Belczynski 2014) to ensure several detections per year with ongoing surveys, such as the Zwicky Transient Facility (ZTF; Adams et al. 2018; Howitt et al. 2020). However, few are likely to happen as close as M31. The event we discuss here, M31-LRN-2015, is probably the closest extragalactic example of this transient family for the next 20 yr, and thus provides the best opportunity for studying the evolution of the remnant at late times.

M31-LRN-2015 was discovered in the Andromeda galaxy (M31) at $\alpha_{J2000} = 00^h42^m07^s.99$, $\delta_{J2000} = +40°55'01''.1$ (6.8 arcmin west and −21.13 arcmin south of its galaxy centre) on UTC 2015 January 13.63 by the MASTER survey (Shumkov et al. 2015a). Though the

transient was initially classified as a classical nova peaking at $R \sim 15.1$ mag, it quickly evolved towards red colours and was re-classified as a LRN based on its luminosity, slow decline, colour evolution, and spectroscopic similarities to V838 Mon by Kurtenkov et al. (2015b). Dong et al. (2015) identified a progenitor in archival *Hubble Space Telescope* (*HST*) imaging and noted that the progenitor had started brightening in later archival Canada France Hawaii Telescope (CFHT) photometry. Kurtenkov et al. (2015a), Williams et al. (2015), and Lipunov et al. (2017) presented optical and near-infrared (NIR) light curves and optical spectra of the outburst spanning from ∼10 d pre-maximum to ∼60 d post-maximum.

Further analysis by MacLeod et al. (2017) used the archival photometry from Dong et al. (2015) and Williams et al. (2015) to estimate the evolutionary stage of the progenitor star for single stellar models. The best agreement was for a 3–5.5 $M_{\odot}$ subgiant star with a radius 30–40 $R_{\odot}$, which was evolving off the main sequence. In their model, the optical transient lasted less than 10 orbits of the original binary, and the light curve was best explained by ∼10^{-2} $M_{\odot}$ of fast ejecta driven by shocks at the onset of CE followed by H recombination of an additional ∼0.3 $M_{\odot}$ of material ejected at slower velocities as the secondary continued to spiral in through the envelope of the primary.

Similar results were obtained by Lipunov et al. (2017), using hydrodynamic simulations designed to reproduce the multicolour light curve of the transient. The observed ∼50-d plateau was explained by a stellar merger with a progenitor mass of 3 $M_{\odot}$ and a radius of 10 $R_{\odot}$, which underwent fast shock heating at the base of the envelope accelerating the matter to photospheric velocities of $v \sim 900$ km s^{-1}. In this scenario, the system is already a tight binary with a degenerate dwarf primary, and the unstable mass transfer is initiated by the secondary companion.

Alternatively, Metzger & Pejcha (2017) suggested that the M31-LRN-2015 had a more extended period of mass-loss from the L2 point before the outburst, which powered the emission observed prior to the main peak. The light curve could then be explained by the release of thermal energy near the peak, followed by a plateau powered by the interaction of a dynamically ejected shell with the pre-existing equatorial material.

In this paper, we present new optical and IR photometry, and optical spectroscopic data on M31-LRN-2015. We investigate the evolution of the progenitor up to 5.5 yr before the outburst, which shows a more complex behaviour. We also provide the first analysis of the remnant, based on IR photometry, taken up to 5 yr after the outburst. We present new observational data in Section 2. Our analysis of the object's spectroscopic and photometric evolution is in Section 3. We discuss the implications of our results in Section 4 and summarize our conclusions in Section 5.

2 OBSERVATIONS

2.1 Distance and reddening

Following Williams et al. (2015) and Lipunov et al. (2017) we adopt a distance of 0.762 Mpc, corresponding to a distance modulus of ($m − M$) = 24.4 mag (Freedman & Madore 1990).

There is some uncertainty in the reddening that should be adopted for M31-LRN-2015. Based on the foreground reddening of $E(B − V) = 0.062$ mag (Schlegel, Finkbeiner & Davis 1998) and the total line-of-sight extinction at the position of M31-LRN-2015 of $E(B − V) = 0.18$ (Montalto et al. 2009), Williams et al. (2015) and Lipunov et al. (2017) assume M31-LRN-2015 was reddened by $E(B − V) = 0.12 \pm 0.06$ mag. Kurtenkov et al. (2015a) report

Table 1. Archival (see references) and follow-up photometry for M31-LRN-2015.

Phase	MJD	Telescope	Filter	Magnitude	ATel
−3810.7	53233	*HST*	*I*	22.02 ± 0.01	7173
−3810.7	53233	*HST*	*V*	23.2 ± 0.03	7173
−3443.7	53600	*Spitzer*	3.6	>17.99	
−3443.7	53600	*Spitzer*	4.5	>17.83	
−3443.7	53600	*Spitzer*	5.8	>17.03	
−3443.7	53600	*Spitzer*	8.0	>15.89	
...	...	...	...	...	...
1260.8	58304.5	Keck	*K*	>24.26	
1291.8	58335.5	Keck	*J*	>25.27	
1291.8	58335.5	Keck	*H*	>24.81	
1793.2	58836.9	*Spitzer*	3.6	>17.2	
1793.2	58836.9	*Spitzer*	4.5	15.73 ± 0.02	

Reference. ATel 7173 (Dong et al. 2015). These values have not been corrected for extinction. This table is shown as a guidance on the format. The ellipsis indicate incomplete data. The full table is available as part of the online material.

a line-of-sight reddening of $E(B - V) = 0.42 \pm 0.03$ mag based on dust maps of M31 (Draine et al. 2014), and find $E(B - V) = 0.35 \pm 0.10$ mag from modelling spectra taken between UTC 2015 January 15 and February 24. In this paper, we adopt a foreground extinction of $E(B - V) = 0.055$ based on the Schlafly et al. (2012) recalibration of the Schlegel et al. (1998) dust maps plus an average host extinction of $E(B - V) = 0.2$, which is a compromise between all previous studies. Therefore, the total extinction used in this study is $E(B - V) = 0.255$.

2.2 Photometry

We monitored the photometric and spectroscopic evolution of M31-LRN-2015 with a variety of ground-based facilities and with the *Spitzer Space Telescope* (*SST*; Werner et al. 2004; Gehrz et al. 2007). We also collected all the published data on this source from literature. A full log of archival and follow-up photometry is shown in Table 1.

The precursor and the nova photometry were retrieved from archival images from the Palomar Transient Facility (PTF; Law et al. 2009; Rau et al. 2009) and the Intermediate Palomar Transient Facility (iPTF; Kulkarni 2013). The images were obtained between MJDs 55569.0 and 57642.0 (5.3 prior to discovery to 1.6 yr after) with the CFH12K camera (Rahmer et al. 2008; Law et al. 2010) on the Palomar 48-inch Telescope (P48). The PTF/iPTF data were processed with the PTF image subtraction pipeline PTFIDE (Masci et al. 2017). The CFHT/MegaPrime light curves with ~6- and ~26-min cadence were obtained from three full nights monitoring the field for microlensing on 2014 October 24, 28, and 30 (PI: Subo Dong). The photometry was obtained using difference imaging analysis (Wozniak 2000) and calibrated using the Pan-STARRS DR1 (PS1; Chambers et al. 2016).

Optical follow-up imaging was obtained with the Liverpool Telescope (Bersier et al. 2015) and with the Large Binocular Camera (LBC; Giallongo et al. 2008) on the Large Binocular Telescope (LBT; Hill, Green & Slagle 2006).

NIR imaging was collected with the LBT NIR-Spectroscopic Utility with Camera and Integral-Field Unit for Extragalactic Research (LUCIFER; Seifert et al. 2003), with the CAmara INfrarroja (CAIN) on the Telescopio Carlos Sánchez and, at late times, with the NIRC2-AO camera on the 10-m Keck II telescope. The observations were made with *J*, *H*, and K_s filters in the wide camera mode, having 40 mas pixel⁻¹. We used the laser guide star adaptative optics (LGS AO;
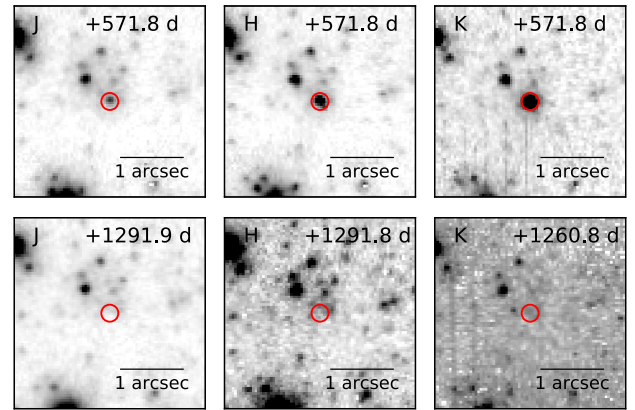

Figure 1. Late-time follow-up of M31-LRN-2015 in *J*, *H*, and K_s bands with Keck II/NIRC2-AO. The location of the target is indicated with a red circle. The remnant is clearly detected at 571.8 d (~1.5 yr), but at 1291.9 d, the star has faded beyond the confusion limit. The cutouts have the standard orientation: north up and east to the left.

Wizinowich et al. 2006) system to obtain diffraction limited images with a full width at half-maximum (FWHM) of approximately 2.5 pixels (equivalent to 0.1 arcsec), required to resolve the fading progenitor in a crowded M31 star field. Fig. 1 shows the location of the outburst 1.5 and 3.5 yr after discovery.

Confusion complicates the interpretation of ground-based (seeing-limited) photometry of the progenitor and remnant. Archival images from *HST* obtained on UTC 2004 August 16 also reveal multiple sources within 1 arcsec of the progenitor with comparable fluxes (Dong et al. 2015; Williams et al. 2015). Image subtraction via the PTFIDE pipeline for the PTF data and via ISIS for the LBT data enables accurate measurement of changes in flux, but not the total flux of the target. However, due to the faintness of the progenitor, we assume that the deviation from the total flux is negligible. The difference imaging precursor light curve is shown in Fig. 2.

In our mid-IR follow-up (Fig. 3), we utilize both new and archival mid-IR data in [3.6] and [4.5] bands from the Infrared Array Camera (IRAC; Fazio et al. 2004) on board *SST*. Under programs 11181, 12063 (PI: C. Kochanek), and 13053, 14089 (PI: M. Kasliwal), we obtained mid-IR imaging from UTC 2015 April 6 to UTC 2019 December 19. We also analysed the archival images from UTC 2005 August 18/19 (program 3126; PI: P. Barmby),[1] and from 2015 taken under the program 11103 (PI: O. Jones). The *Spitzer* photometry was reduced using the difference imaging pipeline developed for the Spitzer InfraRed Intensive Transients Survey (SPIRITS) survey (Kasliwal et al. 2017).

2.3 Spectroscopy

We acquired optical follow-up spectra with the OSMOS spectrograph on the MDM Observatory 2.4-m Hiltner telescope on UTC 2015 March 10 (+ 47.4 d; Wagner et al. 2015) and with the Low Resolution Imaging Spectrograph (LRIS; Oke et al. 1995) on the 10-m Keck I telescope on UTC 2015 June 13 (+142.9 d). The OSMOS spectrum was reduced using standard IRAF routines. The LRIS spectrum was reducing using an IDL-based pipeline LPIPE developed by D. Perley.[2]

---

[1]We do not use archival imaging from this program taken on 2005 January 20/21 because a solar proton event flooded the detector with cosmic rays.
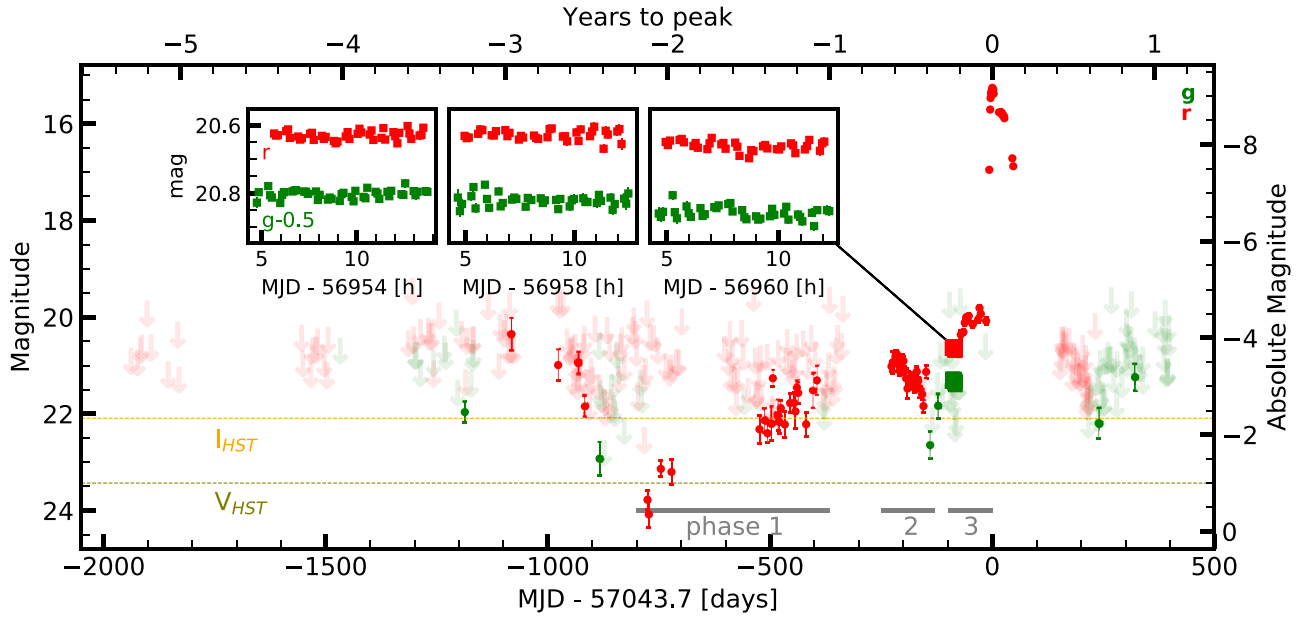[2]http://www.astro.caltech.edu/~dperley/programs/lpipe.html.

Figure 2. PTF/iPTF light curve of M31-LRN-2015 in Mould-*R* (red) and *g* bands (green). The light curve earlier than −20 d has been binned using a bin size of 3 d. At later dates, bins of 1 d were used. The *HST* progenitor limits at MJD 53233 (−10.4 yr) reported by Dong et al. (2015) and Williams et al. (2015) are shown as dashed horizontal lines. The green and red squares show the CFHT photometry. The measurement of the progenitor is reported in Dong et al. (2015). The insets show high-cadence CFHT observations of the field on three full nights at −90, −86, and −64 d before peak. Grey bars in the bottom indicate the different phases of the precursor light curve.
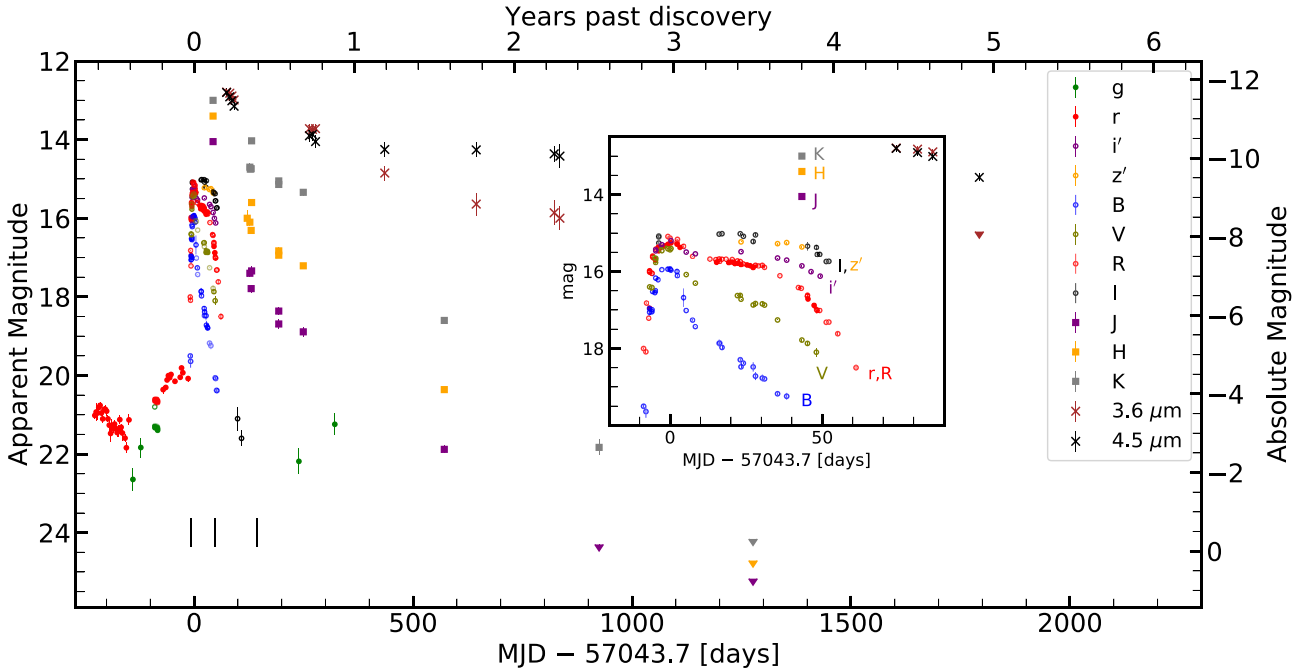
Figure 3. Light curve showing PTF/iPTF photometry, along with our NIR and MIR data. For better clarity, we added the measurements published by Williams et al. (2015) and Kurtenkov et al. (2015a) and ATels (Geier & Pessev 2015; Harmanen et al. 2015; Ovcharov et al. 2015; Srivastava et al. 2015; Steele et al. 2015; Adams et al. 2015a,b; Pessev et al. 2015a,b,c,d; Kurtenkov et al. 2015b; Shumkov et al. 2015b). Downward triangles show upper limits. The inset shows the light curve around peak. The vertical marks under the light curve show the times when our follow-up spectra were obtained. The complete photometry is given in Table 1.

We also include early-time (8 d pre-peak) spectroscopy from WHT/ACAM reported by Hodgkin et al. (2015), the Liverpool Telescope SPRAT Spectroscopy published in Williams et al. (2015), and spectroscopy from Kurtenkov et al. (2015a), constituting the most complete spectroscopic data set up to date. The ACAM spectrum was reduced using the usual IRAF procedures, and scaled using the photometry in *B* and *R* bands of the nova reported for the same night by Kurtenkov et al. (2015a). The observation log for the

Table 2. Log of spectroscopic observations of M31-LRN-2015.

Phase[a] (d)	MJD	UTC	Telescope + instrument	Slit (arcsec)	Exposure (s)	Airmass	Resolution (km s^{-1})	Hel. vel. (km s^{-1})
−7.8	57035.88	2015-01-13T21:05:06	WHT + ACAM	1.5	1200	1.25	880	− 25.6
+47.4	57091.11	2015-03-10T02:44:47	MDM + OSMOS	1.2	600	2.6	190	− 16.2
+142.9	57186.58	2015-06-13T13:58:18	Keck I + LRIS	1.0	590	1.6	300	19.5

Note. [a]The phase is relative to *r*-band peak date with MJD 57043.7.
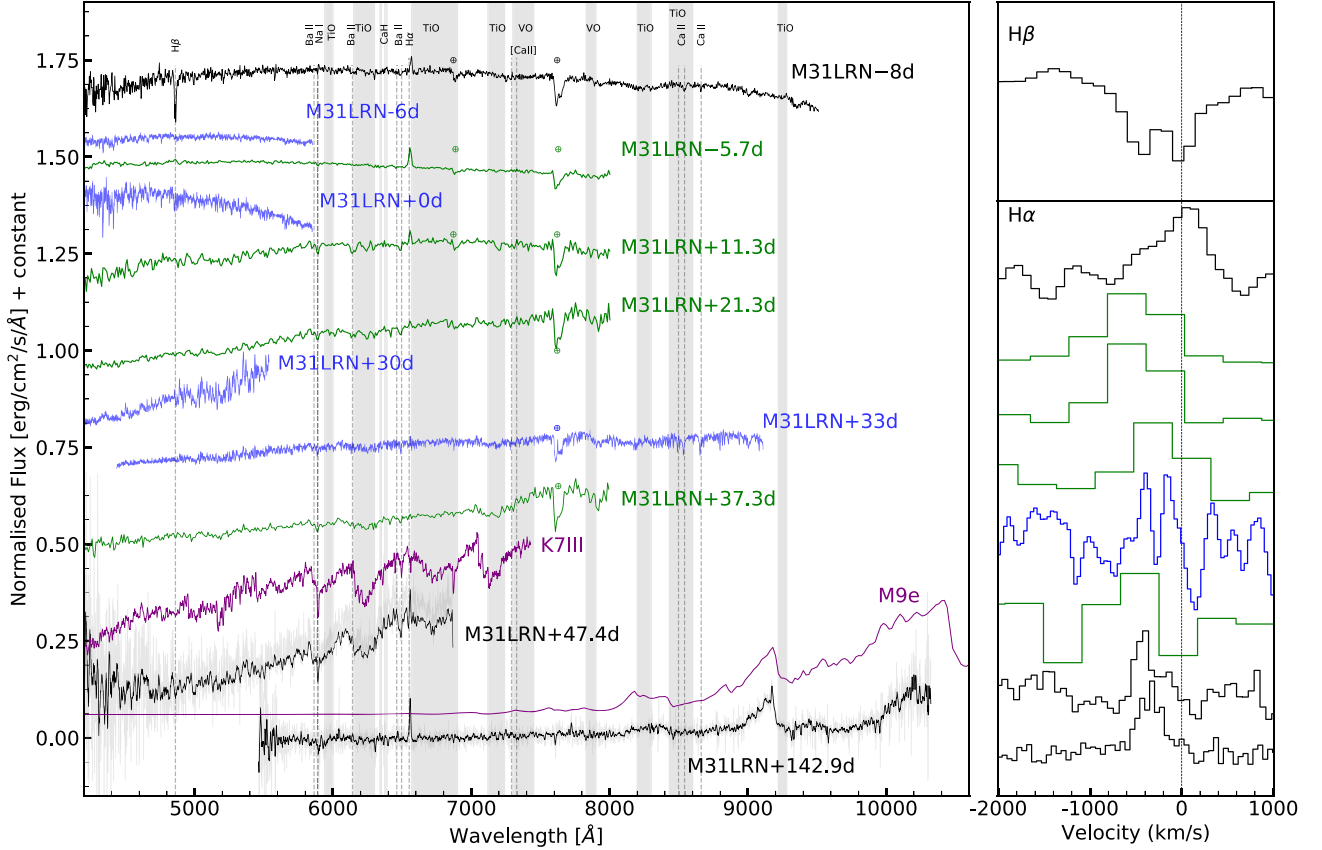
Figure 4. Left-hand panel: optical spectral sequence for M31-LRN-2015. The object spectra are colour coded by source. Our follow-up spectra are shown in black. A K7III spectrum (Jacoby, Hunter & Christian 1984) and M9e (Gunn & Stryker 1983) stellar spectra are shown in purple for comparison. As part of the sequence, we also included in green the LT spectra from Williams et al. (2015) and in blue the spectra from Kurtenkov et al. (2015a). The main element lines have been identified with dashed vertical lines. Molecular absorption bands are shown with grey rectangles. Right-hand panel: continuum-subtracted and peak-normalized profiles for the H β and H α lines.

unpublished spectra is provided in Table 2 and the spectral sequence is displayed in Fig. 4.

In order to correct the spectra for the systemic velocity of Andromeda, we adopt $v_{sys} = -304.5 \pm 6.8$ km s^{-1} (Chemin, Carignan & Foster 2009). In addition, the transient is nearly aligned with the semimajor axis of M31 (6.8 arcmin west and 21.13 arcmin south of M31 centre). Assuming that the progenitor is a relatively young star (100 Myr for a 5 M$_\odot$) that still follows the galaxy rotation curve, we estimate that the star may have an additional correction, related to its rotation within the galaxy of $v_{rot} \sim -200$ km s^{-1}, which should be considered as an upper limit for any additional correction to the velocity.

3 ANALYSIS

3.1 Spectroscopic evolution

Our earliest spectrum was taken 8 d before optical peak. The fit for an extinction-corrected continuum shows an ∼5000-K blackbody emission along with narrow absorption lines for low-ionization elements such as Na I, Fe II, Sc II, and Ba II. We also detect the Ca II triplet in absorption with a velocity of −130 km s^{-1}. Note the lack of emission lines for [Ca II], which are consistently observed in 2008S-like transients (Bond et al. 2009; Botticella et al. 2009) (see Fig. 4). The peak of the H α emission is located at 6558.8 Å, indicating a redshift of ∼100 km s^{-1}. Although the line shows a

Table 3. Fit parameters for the H α and H β lines.

Phase (d)	Ion	Velocity$_e$ (km s^{-1})	FWHM$_e$ (km s^{-1})	Velocity$_a$ (km s^{-1})	FWHM$_a$ (km s^{-1})
−8	H β	–	–	− 48 ± 1	380 ± 247
−8	H α	96 ± 30	<880	–	–
+47.4	H α	− 309 ± 1	115 ± 30	− 553 ± 14	136 ± 22
+142.9	H α	− 304 ± 1	300 ± 20	–	–

Notes. The FWHM have been corrected for instrumental profile. The line fits were corrected for heliocentric velocity and for the systemic velocity of M31. The index 'e' indicates the line emission component and the index 'a' the absorption one.

multicomponent profile, the FWHM of the emission indicates that the line is likely unresolved (<880 km s^{-1}). The H β line is detected in absorption, centred on 4855.7 Å (-50 km s^{-1}) with an FWHM of 380 ± 247 km s^{-1} (see Table 3 for the fit parameters). The profile appears to be partly filled by an emission component, in agreement with the characteristics of the spectrum at -6 d reported by Fabrika et al. (2015) and Kurtenkov et al. (2015a).

The spectral sequences from Williams et al. (2015) and Kurtenkov et al. (2015a) show a quick progression (over ∼40 d) from an almost featureless spectrum into a one dominated by strong absorption bands from recently formed molecules. The H α emission line detected at early times seems to disappear between +11 and +37 d, which coincides with the duration of the light-curve plateau (see Fig. 3). If the plateau is powered by recombination, this process must be occurring deeper in the ejecta, with any emission from hydrogen recombination being absorbed by the cooler outer shell.

Towards the end of the *r*-band plateau at +47 d, the spectrum resembles a K7III star, with strong Na I and Ba II absorption lines and TiO molecular absorption bands. The spectrum again shows the H α line in emission, although its peak has shifted to ∼−300 km s^{-1}. This line likely comes from an expanding, cooling shell. Analogous to cool Mira stars (Kamiński et al. 2017), the emission is accompanied by absorption at +200 km s^{-1}, pointing to the existence of inflowing gas.

The final spectrum, taken on the decline of the plateau, shows an almost complete lack of continuum emission bluewards of 8000Å, as the optical part of the spectrum has been totally absorbed by molecules, such as TiO, VO, and ZrO, which are produced in O-rich atmospheres. The late-time spectrum closely resembles the spectrum of the Mira star R Leo, classified at minimum as having an M9e spectral type (Keenan, Garrison & Deutsch 1974; Gunn & Stryker 1983). The H α line is still present in emission with a similar blueshifted velocity and signs of an absorption profile at a similar velocity.

3.2 Spectroscopic comparison

In the context of stellar mergers, the spectroscopic evolution of M31-LRN-2015 appears closer to the events detected in our own Galaxy than the more luminous transients recently presented by Pastorello et al. (2019b). This last group, mainly consisting of mergers of more massive stars, usually displayed two peaks in their light curve: a first, fast blue peak and a second, slower red peak, which sometimes is smoothed into a pleateau.

A comparison of the pre-peak spectra of M31-LRN-2015 with the extragalactic transient AT2017jfs (Pastorello et al. 2019a; see Fig. 5) shows an initial difference in the continuum temperature, which is also reflected in the emission lines seen during the first peak. AT2017jfs has an initial temperature corresponding to an ionized gas (≥ 7000 K) and the spectrum shows signatures of interaction

with an optically thick circumstellar medium (CSM), due to the strong electron scattering wings on the Balmer lines, Ca II and Fe II. On the other hand, the lower temperature of M31-LRN-2015 (∼5000 K) corresponds to mostly neutral gas and shows the same elements in absorption. The H α and H β emission is likely related to recombination in an optically thin shell, surrounding the main outburst.

The evolution towards colder temperatures is similar to V838 Mon, where we see the appearance of TiO molecular absorption features. The H α line, which disappeared between 11 and 37 d, starts to become detectable again at 47 d. We see very different signatures for spectra of 2008S-like transients taken at a similar phase. For example, M51 OT2019-1 (Jencson et al. 2019a) shows a much hotter continuum, and broadened Balmer emission lines due to electron scattering. These transients also show the Ca II λλ3933, 3968 doublet in absorption, where de-excitation leads to emission in the Ca NIR triplet, followed by a final forbidden transition of [Ca II] λλ7291, 7323. This emission is not detected in LRNe.

The late-time spectrum of M31-LRN-2015 is analogous to other Galactic (V1309 Sco; Kamiński et al. 2015) and extragalactic (M101-OT2015; Blagorodnova et al. 2017) stellar mergers. The cold stellar photosphere shows almost no flux at wavelengths shorter than 7000 Å, and the spectrum is dominated by molecular absorption features. Some low-ionization elements are detected as narrow emission lines, likely generated in an optically thin shell irradiated by unobscured emission from the central object. The increased optical depth due to formation of dust can also explain the blueshift commonly observed in the the H α profiles.

3.3 Constraints on progenitor dust

Based on the archival SDSS and CFHT imaging data presented in Dong et al. (2015), we argue that the progenitor star had a relatively constant optical luminosity between 2002 and 2009. The photometry derived for this period agrees with the *HST* magnitudes $V = 23.2 \pm 0.03$ and $I = 22.02 \pm 0.01$ in 2004, about 10.4 yr before the outburst peak (Dong et al. 2015; Williams et al. 2015). The constant luminosity of the progenitor allows us to combine the optical data with *Spitzer* upper limits obtained 9.4 yr before the outburst to place constraints on the pre-existing dust in the system.

Our simple progenitor model assumes optically thin dust of uniform grain size $a = 0.1\ \mu$m, which radiates at a single equilibrium temperature T_d. Given the abundance of oxygen-rich molecules in the ejecta of LRNe, we assume silicate dust for our analysis. The assumption of a different dust composition does not significantly alter our results.

The specific luminosity for a dust grain of radius a and temperature T_d radiating at wavelength λ is given by

$$l_\nu(\lambda) = 4\pi a^2 B_\nu(\lambda, T_d) Q_{ext}(\lambda), \qquad (1)$$

where $B_\nu(\lambda, T_d)$ is the Plank function, and $Q_{ext} = Q_{abs} + Q_{sca}$ is the dust efficiency factor for extinction (absorption plus scattering). For silicate dust, we use the tabulated values of Laor & Draine (1993).[3] Introducing the dust opacity, $\kappa(\lambda, a) = 3Q_{ext}(\lambda)/4\rho_d a$, where ρ_d is the dust bulk density ($\rho_d = 2.2$ g cm^{-3} for graphitic dust and 3.5 g cm^{-3} for silicate), we can rewrite the equation as

$$l_\nu(\lambda) = 4M_d\pi B_\nu(\lambda, T_d)\kappa(\lambda, a), \qquad (2)$$

---

[3] Available from https://www.astro.princeton.edu/~draine/dust/dust.diel.html.
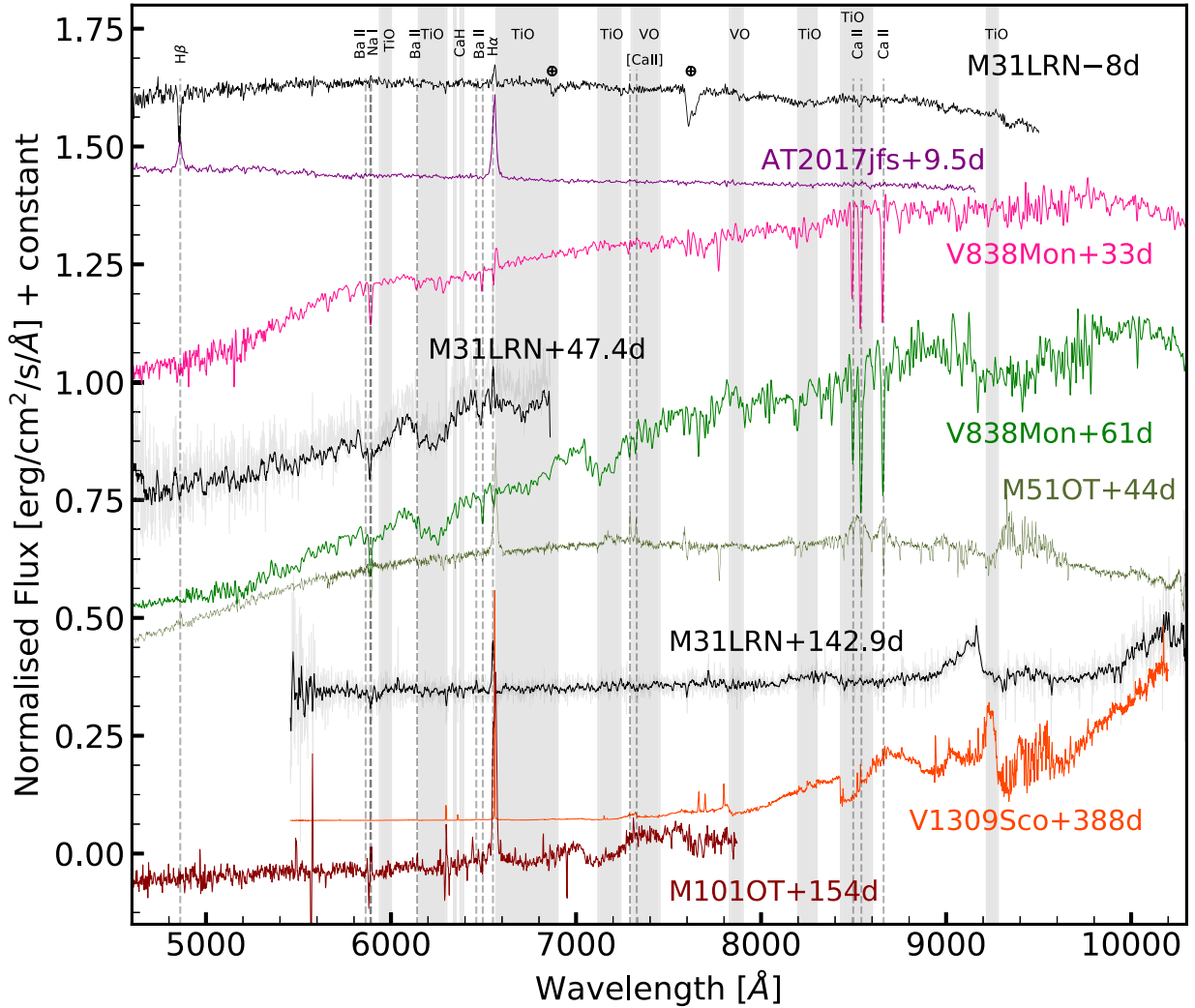
Figure 5. Spectral evolution of M31-LRN-2015 (shown in black) compared to other 'gap' transients at similar epochs. The spectra of the massive stellar merger AT2017jfs (Pastorello et al. 2019a) during the first peak are shown in purple, the intermediate-mass merger V838 Mon (Smith et al. 2016) in shown in pink and green, the 2008S-like transient M51-OT2019 (Jencson et al. 2019a) is shown in olive, the low-mass merger V1309 Sco (Kamiński et al. 2015) in shown in orange, and the massive merger M101-OT2015 (Blagorodnova et al. 2017) in shown in brown.

where M_d is the dust mass. The flux density for an observer at distance d is

$$F_\nu(\lambda) = \frac{M_d B_\nu(\lambda, T_d)\kappa(\lambda, a)}{d^2}. \tag{3}$$

For our analysis of the progenitor SED, we initially fit the optical *HST* magnitudes with a single blackbody to estimate its contribution to the mid-IR flux. The best fit given by our extinction is $T = 4336^{+41}_{-43}$ K, $R = 46^{+2}_{-1} R_\odot$, and bolometric luminosity $L = 681^{+64}_{-53} L_\odot$. Next, for each dust temperature $50 \leq T_d \leq 1500$ K, we derive the maximum dust mass M_d, which is still consistent with a non-detection.

Our results, depicted in Fig. 6, show that although the temperature has a strong influence on the dust mass, we still can place meaningful constraints for warmer dust. For example, for the hottest temperatures of $T_d = 1000$–1500, we find that $M_d < (10^{-9.2}$–$10^{-9.7}) M_\odot$ and for $T_d = 500$ K, $M_d < 10^{-8.0} M_\odot$. For temperatures of 300 and 100 K, the peak of the emission shifts further into the far-IR, increasing the limits to $10^{-6.9}$ and $10^{-1.7} M_\odot$. Due to the lack of far-IR measurements, our limits for colder dust are not that constraining, so we can not rule out

the presence of a cold ($\sim$30 K) dust shell, such as the one detected for the remnant of V1309 Sco (Tylenda & Kamiński 2016).

3.4 Pre-outburst progenitor evolution

The extensive coverage of M31 by CFHT and the PTF/iPTF surveys since 2010 provides enough data to study the evolution of the progenitor up to 5 yr before its outburst. Using the PTFIDE pipeline, we obtained hundreds of forced photometry measurements for observations taken between 2010 and the onset of the nova in 2015 January, as shown in Fig. 2. The Mould-*R*-band luminosity remained mostly below our detection threshold up to 2 yr before the outburst. After that, in what we call phase 1, it steadily increased in brightness by nearly 2 mag between −2 and −1 yr. During phase 2, at the start of the 2014 summer (−250 d), the progenitor was an additional magnitude brighter than in spring 2014, but faded by nearly a magnitude over the next three months. During phase 3, starting about 150 d prior to the 2015 January outburst, the Mould-*R* band flux reached its overall maximum of $\sim$20 mag and then remained relatively steady, with some minor fluctuations.
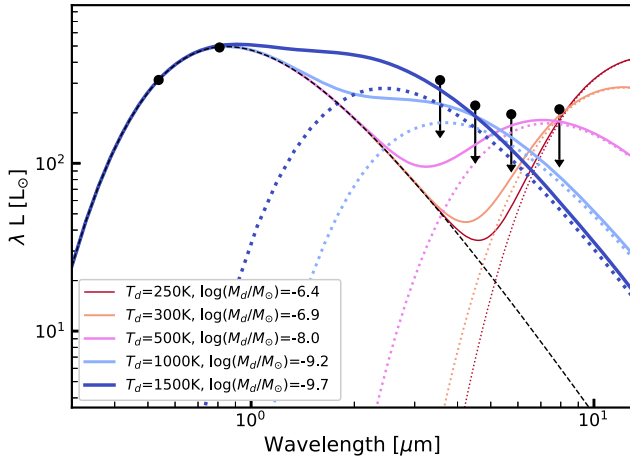
Figure 6. Limits for silicate ($a = 0.1\,\mu$m) dust emission component in the progenitor SED. The black points indicate the optical photometric measurements and the IR upper limits. The black dashed line shows the blackbody fit to the progenitor photometry. The coloured dashed lines show the dust emission model at different temperatures T_d for a maximum dust mass M_d. Solid lines of the same colour indicate the total flux emitted by the star and the dust.

Figure 7. Left-hand panel: 3-d binned *R*-band light curve for phase 2 (top panels) and the folded light curve using the best average period of 16.8 d (bottom panels). Right-hand panels: 3-d binned light curve for phase 3 (top panels) and folded light curve with a period of 28.1 d (bottom panels). The error bars in the *x*-axis represent the width of the bin. All panels show the best linear polynomial fit used to remove the continuum, as well as the model light curve for the corresponding period.

CFHT data taken at about three months before eruption (Dong et al. 2015) agrees with iPTF observations (see insets in Fig. 3). A single blackbody fit to the g- and r-band SED shows that the temperature of the emission was 6300^{+500}_{-500} K with a radius of $55^{+10}_{-10}\,R_\odot$, which indicates that the precursor emission became hotter than the progenitor and its photospheric radius increased. The lack of extensive simultaneous multiband photometry during the whole precursor period makes it difficult to determine whether the optical luminosity is linked to the apparent expansion and cooling of the photosphere, similar to the behaviour displayed by other stellar mergers such as V1309 Sco (Pejcha et al. 2017) or M101-2015OT (Blagorodnova et al. 2017), or to tidal heating (MacLeod et al. 2017), where the atmosphere of the primary star is disturbed by the secondary. Like other stellar mergers, M31-LRN-2015 also shows a smooth, monotonic brightening lasting about 2 yr. After this, the light curve also shows a dip, followed by a short precursor, similar to the one observed for V838 Mon (Munari et al. 2002) or V1309 Sco. This behaviour is likely too complex to be caused by tidal heating. A possible explanation is the loss of mass from the system through the the L2 point during the RLOF, as proposed by Pejcha et al. (2017).

Mass-loss progressively drains angular momentum from the binary, which causes the orbit to shrink. The outflowing gas can then form an expanding photosphere around the binary. Pejcha et al. (2017) showed that the slow rise of V1309 Sco for thousands of orbits prior to merger could be explained by such dynamical mass-loss. Assuming that the brightening in phase 1 of M31-LRN-2015 is due to an expanding optically thick outflow, we would expect the luminosity to scale as $L \propto (\dot{P}/P)^2 \propto (\dot{M}/M)^2$, where P is the period of the system. As the mass-loss increases, the outflow is expected to completely engulf the binary, thereby causing the luminosity to decrease (phase 2). The observed emission now comes from shock interactions created by the L2 outflow. Depending on the binary mass ratio, further mass-loss from the system can either form an expanding photosphere, or be marginally bound to the binary and interact with it. Either of these scenarios leads to a gradual increase in the luminosity (phase 3), as the
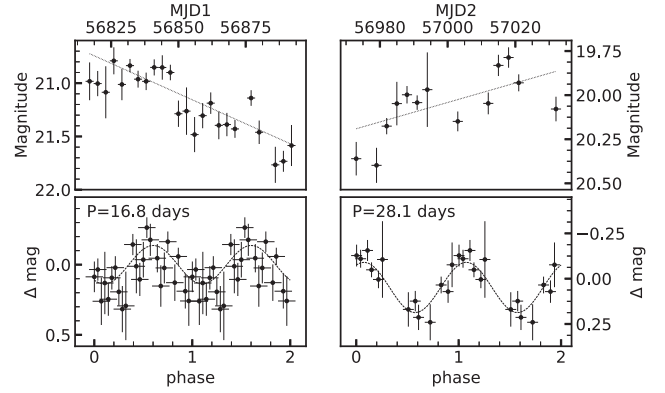
orbit shrinks further until the binary finally merges, leading to the outburst.

Though the general trend of the M31-LRN-2015 light curve is similar to that of the V1309 Sco, there are a few differences. The most prominent difference is that the pre-outburst brightening of V1309 Sco smoothly transitioned into the outburst, with the photosphere expanding $\propto \dot{P}/P$, whereas for M31-LRN-2015, the pre-outburst brightening reached a constant value before the main outburst. In this regard, M31-LRN-2015 is more similar to V838 Mon. Before its first eruption, V838 Mon brightened by more than 3 mags and plateaued for around 25 d (Munari et al. 2002). Tylenda (2005) found that during this phase, the photospheric radius of V838 Mon remained almost the same. This could occur if the mass ejected during the brightening is marginally bound, and falls back to interact with the binary (Pejcha et al. 2016b). For outflows launched in synchronicity with the binary, a necessary, but not sufficient, condition is the binary mass ratio q to be < 0.064 or > 0.78.

Close inspection of phases 2 and 3 shows that the residuals seem to be correlated once the general trend is removed, as the scatter in our measurements is larger than the error bars (the uncertainties for phase 1 are too large for a reliable analysis). Similar characteristics were observed for V1309 Sco (Pejcha et al. 2017), where the amplitude of the residuals oscillated by 0.3 mag. Deviations from the $(\dot{P}/P)^2$ rise were observed, but no period could be determined for the residuals. These residuals were interpreted as being due to the clumpiness and asymmetry of the mass lost from the binary. Motivated by the apparent correlation, we tested our light curve for periodicity in phases 2 (between MJD 56800–56895) and 3 (MJD 56960–57035). After removing a linear trend from our data, we used the Lomb–Scargle (Lomb 1976; Scargle 1982) algorithm, to produce a periodogram using different binnings and offsets of the bins. For phase 2, none of our best fits exceeded a power of 0.5, indicating a low significance for any period. However, the results consistently show one best period around 17 d (see Fig. 7). Averaging all the periods for binnings from 1 to 4 d (weighted by their power) allows us to derive a possible period of 16.8 ± 0.3 d. For phase 3, the power increases above 0.7. The average period for this phase is 28.1 ± 1.4 d, nearly double than for phase 2.

If the period detected in phase 2 is real, its variability can be used to infer the characteristics of the binary system. MacLeod et al. (2017)

derived a mass of 3–5.5 M$_\odot$ and a radius of 28–35 R$_\odot$ for the primary (depending on reddening). The period of a test mass at the surface of this binary is 13–7 d depending on the mass and radius. However, if the primary is undergoing RLOF, the inferred radius corresponds to the Roche lobe of the primary. For our extinction value of $E(B - V) = 0.255$, the primary has $M_1 = 5$ M$_\odot$ and $R_1 = 32$ R$_\odot$. The period for the binary for a mass ratio of $0.01 \leq q \leq 1$ ($q = M_2/M_1$) is in the range of 15–28 d.

Our first period of $\simeq 16.8$ d would be in agreement with RLOF scenario with $q \simeq 0.03$. However, an ellipsoidal variation would actually imply a period twice as large, which is outside the expected range we just derived. Our second period of $\simeq 28$ d requires the binary to be of nearly equal mass. Ideally, earlier stages of the light curve would have provided an independent verification of the variability, but this is not possible due to the low S/N of the individual detections in our data.

The detection of periodicity at later stages of the light curve is nevertheless surprising, as the binary is expected to be completely engulfed at this point. For example, an apparent increase in the period was observed in the early phases of the V1309 Sco light curve, when the phased light curve changed from a double hump profile to a single hump, effectively doubling the detected period from 0.7 to 1.4 d (Tylenda et al. 2011). This doubling of the period was attributed to the asymmetric nature of the L2 mass-loss, in that the ejected mass trailed around the binary and partly obscured the system. Provided the period for M31-LRN-2015 has increased by nearly a factor of 2 from phase 2 to phase 3, it could possibly be a manifestation of the same phenomenon as in V1309 Sco. It is also likely that the binary is, in fact, completely engulfed by the dust at this point, and the observed period is a result of interactions in the L2 mass outflow, as analysed for the light curve of V1309 Sco (Pejcha 2014).

3.5 Post-outburst remnant evolution

The late time photometric evolution of M31-LRN-2015 was monitored in the IR by a combination of ground and space telescopes, as detailed in Section 2.2. In order to analyse the SEDs of the transient, we fixed the times and values for the NIR observations, and linearly interpolated the *Spitzer* and optical observations to those epochs. In total, we obtained the SED for seven post-peak epochs from at 43 d up to ~3.5 yr post peak.

Following the methods of Adams & Kochanek (2015) and Adams et al. (2016, 2017), we modelled the SEDs with the dusty radiative transfer code DUSTY (Ivezic & Elitzur 1997; Ivezic, Nenkova & Elitzur 1999; Elitzur & Ivezić 2001). In these models, DUSTY is embedded in a Markov chain Monte Carlo (MCMC) wrapper to estimate the model parameters and their uncertainties. For the central source, we assume a blackbody radiation with a uniform prior on the temperature of $2500 \leq T_* \leq 20\,000$ K. The dust is treated as a shell with density profile $\rho \propto r^{-2}$. We assume that the shell was launched on the date of discovery (2015 January 14), when the object brightened significantly. The velocity of the shell, v_{ej}, is computed as the ratio between the outer radius and the time elapsed since its ejection. In our analysis, we fix the outer radius of the dust shell to be twice the inner dust radius, R_{in}. The temperature of the dust at the inner radius is T_* and at the outer radius is T_d. We examine optical depth values in the visual band within the range $0.0 \leq \tau_V \leq 1000$.

For our analysis, we tried with both silicate and graphitic grains from Draine & Lee (1984). For the dust grain sizes, we assume the standard MRN (Mathis, Rumpl & Nordsieck 1977) distribution function given by $n(a) \propto a^{-q}$, $a_{min} < a < a_{max}$ with $q = 3.5$, $a_{min} = 0.005\,\mu$m, and $a_{max} = 0.25\,\mu$m. Finally, the reddening from

the Milky Way and within the host galaxy was included as a fixed parameter with $E(B - V) = 0.255$.

One limitation of our analysis is the assumption of spherical symmetry. Outflows from stellar mergers are likely equatorial, due to previous episodes of mass-loss in the binary orbital plane (Metzger & Pejcha 2017; MacLeod et al. 2018a; Reichardt et al. 2019). Therefore, the estimated dust optical depth could be an over or underestimation depending on the viewing angle.

The best-fitting models for both silicate and graphitic dust analysis are shown in Fig. 8. The model parameters and their 1σ uncertainties are provided in Table 4, and depicted in Fig. 9. Next we highlight the most important results of our analysis.

The dusty analysis of the progenitor SED obtained at -3795 d (10.4 yr prior to the outburst) favours optically thin dust. This is consistent with our analysis in Section 3.5, where, for a dust temperature of $T_d \sim 400$ K, the total dust mass in the system was below 10^{-7} M$_\odot$.

Our earliest full optical to MIR SED is located towards the end of the *r*-band plateau at 43 d. At this stage, the transient is well fitted by a single-component $\simeq 3400$-K blackbody and a radius of 1700 R$_\odot$, which is consistent with the size of the ejecta if assuming that it expanded at a uniform velocity of 300 km s^{-1}. Albeit the evidence of dust at this phase is small (see the 43-d panel in Fig. 8), we discuss the possible implications. If dust is present, it is optically thin and located far from the stellar photosphere. Our spectrum taken at $+47.4$ d already shows signs for TiO absorption, in agreement with a cold stellar temperature. The shell has a dust temperature of $\simeq 1750$ K, which would allow the dust condensation process to take place. If ejected around the discovery date, the large extent of this shell implies a much faster velocity than the velocity of the photosphere, with 1580^{+700}_{-360} km s^{-1}. The most likely scenario is that this shell was already formed during the years or months preceding the eruption. For example, if the gas travelled from the system at the escape velocity of ~250 km s^{-1} (MacLeod et al. 2017), a thin shell could have been ejected ~160 d before the outburst peak, which coincides with the luminosity increase in the transient's light curve (phase 3).

By 127 d, the emission in the optical has almost faded below detection, as the dust shell has become optically thick ($\tau_V \simeq 19$) and has started to reprocess most of the radiation from the obscured remnant. The temperature of the star appears slightly hotter than during the plateau, with $T_* \simeq 4500$ K. The radius of this shell is ~4000 R$_\odot$. Within the errors, this is consistent with the estimates for the previous phase when the shell had to be optically thin. The estimated temperature of this shell is also similar, $T_d \sim 1700$ K, which is close to the threshold for the condensation of O-rich minerals (Lodders 2003).

A couple of months later, at 193 and 249 d, we observe a continuous decrease in the bolometric luminosity of the source. Although the temperature of the star increases to $T_* \sim 7000$ K, the temperature and the inner radius of the dust shell remains relatively constant. Over the first year of observations, the optical depth of the shell also remains stable.

A major change in the system is observed at 571 d (~1.5 yr post-outburst). At this time, the SED has clearly developed two distinct emission components. While the temperature of the central star has risen even further to $T_* \sim 10^4$ K, the temperature of the dust has cooled to ~800 K. The shell also appears four times larger than before with $R_{in} \sim 1.6 \times 10^4$ R$_\odot$.

After this phase, our last two epochs taken at 2.5 and 3.5 yr show that the star possibly maintains a temperature of ~10^4 K. The lack
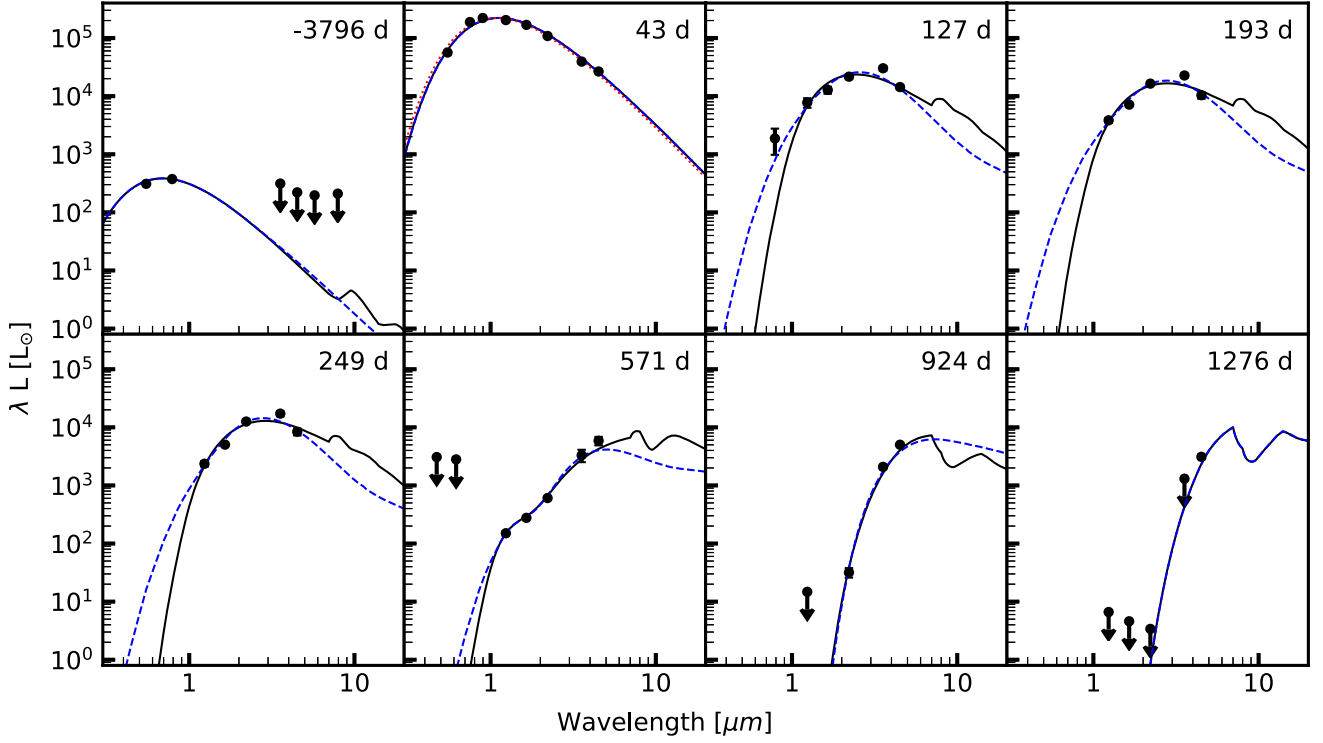
Figure 8. Evolution of the SED of M31-LRN-2015 with phases measured relative to MJD 57043.7. The SEDs in this figure have been corrected for foreground extinction of $E(B-V) = 0.255$. The black solid line shows the best-fitting silicate DUSTY model and the blue dashed line shows the best-fitting graphitic model. The red dotted line at 43 d shows the contribution of a blackbody alone.

Table 4. Posterior parameter from DUSTY MCMC models of the remnant SED.

Dust model	Date (UTC)	Phase (d)	$\log(L_*/L_\odot)$	T_* (K)	$\tau_{V, \text{tot}}$	$\log(R_{\text{in}}/\text{cm})$	T_d (K)	$\log(v_{\text{ej}}/\text{km s}^{-1})$	$\chi^2_{\min}$	M_{ej} (M$_\odot$)
Silicate	2004-08-16	−3811	$2.78^{+0.09}_{-0.04}$	5850^{+900}_{-660}	$0.8^{+0.8}_{-0.5}$	$14.48^{+0.29}_{-0.29}$	440^{+220}_{-140}	$2.49^{+0.29}_{-0.29}$	$1.8^{+2.4}_{-1.2}$	$7.8^{+33.5}_{-6.5} \times 10^{-6}$
Silicate	2015-03-06	43	$5.49^{+0.01}_{-0.01}$	3390^{+240}_{-130}	$0.7^{+0.8}_{-0.5}$	$14.54^{+0.16}_{-0.11}$	1760^{+170}_{-250}	$3.2^{+0.16}_{-0.11}$	$12.4^{+3.4}_{-2.3}$	$1.0^{+2.6}_{-0.8} \times 10^{-5}$
Silicate	2015-05-29	127	$4.54^{+0.03}_{-0.02}$	4500^{+3210}_{-1470}	$19.0^{+3.8}_{-5.1}$	$14.4^{+0.15}_{-0.11}$	1740^{+160}_{-190}	$2.63^{+0.15}_{-0.11}$	$26.1^{+3.5}_{-1.7}$	$1.5^{+0.8}_{-0.5} \times 10^{-4}$
Silicate	2015-08-03	193	$4.43^{+0.05}_{-0.03}$	6670^{+4360}_{-2560}	$20.2^{+3.6}_{-5.4}$	$14.47^{+0.19}_{-0.12}$	1680^{+180}_{-180}	$2.53^{+0.19}_{-0.12}$	$32.3^{+3.7}_{-1.9}$	$2.2^{+1.7}_{-0.8} \times 10^{-4}$
Silicate	2015-09-28	249	$4.32^{+0.05}_{-0.03}$	7120^{+4490}_{-2970}	$22.3^{+4.0}_{-5.6}$	$14.43^{+0.2}_{-0.13}$	1680^{+180}_{-200}	$2.38^{+0.2}_{-0.13}$	$28.4^{+3.7}_{-2.0}$	$2.0^{+1.9}_{-0.7} \times 10^{-4}$
Silicate	2016-08-15	571	$4.09^{+0.11}_{-0.09}$	10450^{+2280}_{-1700}	$27.3^{+3.9}_{-4.4}$	$15.07^{+0.13}_{-0.12}$	840^{+50}_{-50}	$2.68^{+0.13}_{-0.12}$	$3.7^{+3.4}_{-2.0}$	$4.7^{+3.7}_{-2.0} \times 10^{-3}$
Silicate	2017-08-03	924	$3.84^{+0.08}_{-0.06}$	9780^{+6200}_{-5090}	$287.2^{+324.7}_{-113.2}$	$14.75^{+0.13}_{-0.08}$	1110^{+210}_{-190}	$2.15^{+0.13}_{-0.08}$	$3.1^{+2.1}_{-0.7}$	$1.3^{+0.9}_{-0.5} \times 10^{-2}$
Silicate	2018-07-21	1276	$4.12^{+0.26}_{-0.19}$	9360^{+6340}_{-4690}	$415.2^{+280.7}_{-157.8}$	$15.3^{+0.26}_{-0.22}$	700^{+150}_{-120}	$2.56^{+0.26}_{-0.22}$	$0.7^{+1.4}_{-0.4}$	$2.1^{+5.3}_{-1.4} \times 10^{-1}$
Graphite	2004-08-16	−3811	$2.79^{+0.08}_{-0.05}$	5840^{+780}_{-600}	$0.3^{+0.3}_{-0.2}$	$14.44^{+0.36}_{-0.34}$	760^{+270}_{-210}	$2.44^{+0.36}_{-0.34}$	$2.5^{+3.1}_{-1.6}$	$2.7^{+12.9}_{-2.2} \times 10^{-6}$
Graphite	2015-03-06	43	$5.48^{+0.01}_{-0.01}$	3410^{+190}_{-130}	$0.2^{+0.3}_{-0.2}$	$14.53^{+0.13}_{-0.08}$	1820^{+120}_{-190}	$3.19^{+0.13}_{-0.08}$	$13.1^{+3.5}_{-2.3}$	$3.9^{+5.8}_{-2.8} \times 10^{-6}$
Graphite	2015-05-29	127	$4.5^{+0.02}_{-0.01}$	5600^{+3810}_{-2110}	$5.6^{+1.7}_{-2.4}$	$14.69^{+0.16}_{-0.13}$	1300^{+140}_{-110}	$2.92^{+0.16}_{-0.13}$	$20.9^{+3.2}_{-2.0}$	$1.6^{+0.5}_{-0.4} \times 10^{-4}$
Graphite	2015-08-03	193	$4.36^{+0.03}_{-0.02}$	6970^{+3930}_{-2520}	$5.5^{+2.1}_{-2.8}$	$14.75^{+0.18}_{-0.14}$	1220^{+100}_{-90}	$2.81^{+0.18}_{-0.14}$	$21.8^{+3.1}_{-1.9}$	$2.0^{+0.7}_{-0.5} \times 10^{-4}$
Graphite	2015-09-28	249	$4.25^{+0.04}_{-0.02}$	7900^{+5070}_{-3320}	$5.7^{+2.8}_{-3.6}$	$14.72^{+0.22}_{-0.16}$	1200^{+110}_{-100}	$2.68^{+0.22}_{-0.16}$	$17.4^{+2.8}_{-0.5}$	$1.8^{+0.6}_{-0.4} \times 10^{-4}$
Graphite	2016-08-15	571	$3.83^{+0.09}_{-0.09}$	7320^{+1070}_{-910}	$11.3^{+1.5}_{-1.5}$	$15.24^{+0.12}_{-0.12}$	670^{+40}_{-40}	$2.84^{+0.12}_{-0.12}$	$5.2^{+3.4}_{-2.0}$	$4.2^{+3.5}_{-1.9} \times 10^{-3}$
Graphite	2017-08-03	924	$3.97^{+0.15}_{-0.16}$	9580^{+5420}_{-4490}	$68.2^{+32.8}_{-8.8}$	$15.0^{+0.35}_{-0.44}$	890^{+350}_{-170}	$2.4^{+0.35}_{-0.44}$	$2.4^{+3.1}_{-1.7}$	$9.5^{+30.6}_{-7.0} \times 10^{-3}$
Graphite	2018-07-21	1276	$4.1^{+0.26}_{-0.2}$	6980^{+6900}_{-3100}	$441.1^{+289.3}_{-184.6}$	$15.28^{+0.26}_{-0.22}$	680^{+130}_{-110}	$2.54^{+0.26}_{-0.22}$	$0.8^{+1.5}_{-0.5}$	$2.0^{+5.3}_{-1.3} \times 10^{-1}$

Notes. The uncertainties give 1σ levels. L_* is the bolometric luminosity of the source, T_* is the intrinsic effective temperature of the input SED, $\tau_{V, \text{tot}}$ is the optical depth of the shell in the V band, and R_{in} is the inner radius of the dust shell, where the dust has temperature T_d. $R_{\text{out}}/R_{\text{in}}$ is the thickness of the dust shell, v_{ej} is the velocity of the shell (assuming a constant expansion rate), χ^2 is the fit of the model, and M_{ej} is the ejecta mass computed using equation (5). For the analysis, we adopted the local $E(B-V) = 0.2$ in M31 in addition to $E(B-V) = 0.055$ for Galactic extinction.
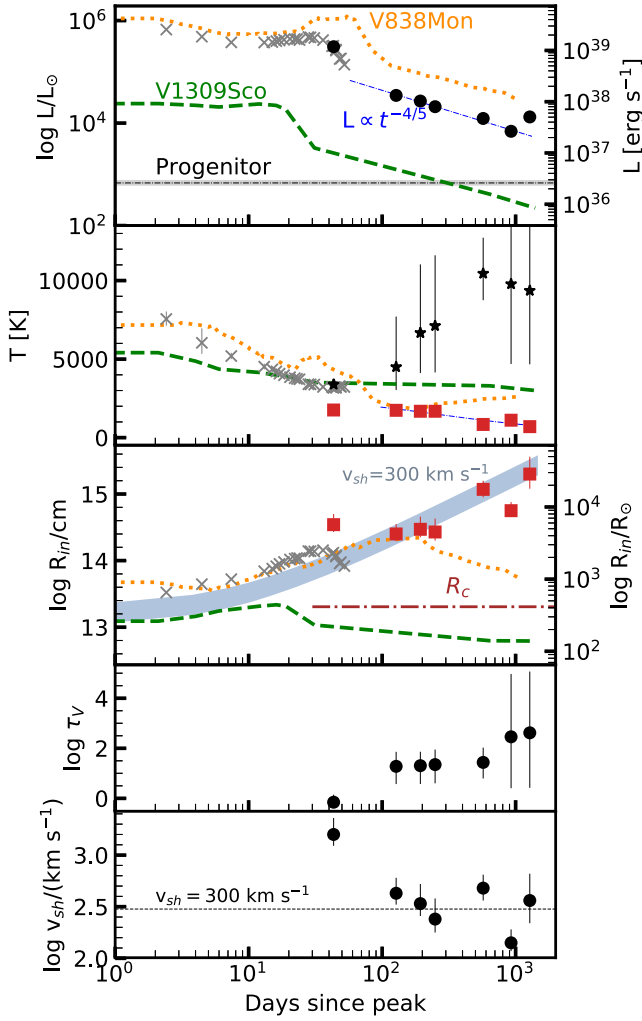
Figure 9. The top panels show the bolometric luminosity of the system (black circles). The progenitor luminosity is marked with a dashed line. The blue line shows the expected gravitational contraction at fixed temperature (equation 11). For context, we also include the evolution of the transient parameters derived from the optical and NIR SEDs by MacLeod et al. (2017, grey crosses). The coloured lines show the evolution for two Galactic stellar mergers (V838 Mon, V1309 Sco; Tylenda 2005; Tylenda et al. 2011; Tylenda & Kamiński 2016), where we match the transients at the time of the first peak. The second panel shows the temperature for our late-time analysis of the remnant star (black stars) and the dust shell (red squares), assuming silicate dust composition. The third panel shows the inner radius of the dust shell. The blue shaded area shows the inner and outer radius of a shell with uniform velocity that would have been ejected at discovery date. The brown line shows the dust condensation radius R_c for the M31-LRN-2015 progenitor. The bottom two panels show the optical depth and the shell expansion velocity.

of optical data makes this temperature mostly dependent on our prior. The dust temperature at 2.5 yr appears slightly warmer than before, ~ 1100 K, and its internal radius shrinks to $R_{in} \sim 8 \times 10^3 \, R_\odot$. However, by 3.5 yr, it cools again to 700 K and expands to its largest value of $R_{in} \sim 3 \times 10^4 \, R_\odot$. The optical depth for these last two epochs is $\tau_V > 200$. Although our analysis for this phase is mostly based on non-detections, we suggest a possible final increase in the total luminosity of the source.

To summarize our analysis, we see that dust formation occurs in three main episodes. First, there is weak evidence for an initial

ejection of gas at ~ 160 d before the outburst, forming an optically thin shell of warm dust present during the post peak plateau.

The second episode takes place during the first 1.5 yr after the outburst. The shell cools slowly, forming a moderate amount of dust ($\tau_V \simeq 20$). Its inner radius is mostly consistent with the location of matter ejected at $v_{sh} \sim 300 \, \mathrm{km\,s^{-1}}$ near the discovery date (see Fig. 9).

The final episode includes epochs later than 2.5 yr. They are characterized by large optical depths, with values $\tau_V > 200$. In the first epoch, there is an apparent shrinkage of the inner radius. This measurement is not in agreement with the expanding shell trend, which may be a limitation of our model due to the limited data on the source's SED. However, if the radius contraction is real, we attribute it to an increase in the dust opacity, perhaps due to the formation of smaller dust grains deeper in the ejecta (see Iaconi et al. 2020) or to an increase in the dust temperature due to shocks. This argument is supported by our last epoch at 3.5 yr: Once the dust has cooled again, the radius seems to return to the trend of an expanding shell. Progressive cooling of the shell allows further dust condensation, increasing its mass up to an order of magnitude (see Table 4).

3.6 Estimate of the ejecta mass

For a shell with total ejecta mass M_{ej} and radius R, the optical depth in the visual band is defined as

$$\tau_V = \frac{\kappa_V M_{ej}}{4\pi R^2} \approx 3.27 \times 10^6 \left(\frac{\kappa_V}{100 \, \mathrm{cm^2\,g^{-1}}}\right) \left(\frac{M_{ej}}{M_\odot}\right) \left(\frac{1000 \, R_\odot}{R}\right)^2. \tag{4}$$

Provided our models fit for τ_V and the shell inner radius, we can estimate the total ejected mass as

$$\frac{M_{ej}}{M_\odot} \approx 3.06 \times 10^{-7} \left(\frac{100 \, \mathrm{cm^2\,g^{-1}}}{\kappa_V}\right) \left(\frac{R}{1000 \, R_\odot}\right)^2 \tau_V. \tag{5}$$

Given that $\kappa_V \sim 50\text{--}100 \, \mathrm{cm^2\,g^{-1}}$ for a typical dust-to-gas ratio (Ossenkopf & Henning 1994), we derive the mass of the shell at different epochs (see Table 4). For our last epoch SED and adopting $\kappa_V = 50 \, \mathrm{cm^2\,g^{-1}}$ we derive $M_{ej} = 0.21^{0.53}_{-0.13} \, M_\odot$, which is consistent with the estimates by Williams et al. (2015) and MacLeod et al. (2017). Nevertheless, this value is likely only a lower limit, as simulations have shown that dust formation continues in the inner regions of the ejecta many years after the outburst has faded (Iaconi et al. 2020).

This estimate brings some tension with the models of Metzger & Pejcha (2017). In their shock powered scenario, the same luminosity would require a substantially lower ejecta mass than the $0.3 \, M_\odot$ derived for a recombination scenario (MacLeod et al. 2017). For shell velocities in the range of $100\text{--}300 \, \mathrm{km\,s^{-1}}$, the ejecta mass would drop by a factor of $\sim (2 \mathrm{Ryd}/(m_p v_{sh}^2)) \sim 3\text{--}30$, requiring at most $0.1 \, M_\odot$. However, assumptions about the gas opacity can introduce large systematic errors in the mass estimates and remove the discrepancy.

4 DISCUSSION

4.1 The origin of the precursor emission

Our observations show an increase in the luminosity prior to the primary transient. One possible origin for the brightening is the dissipation of energy by shocks within the spiral stream that forms around the binary once the gas has left the L2 point. In order to infer the mass-loss required to power this emission, we first reconstruct the
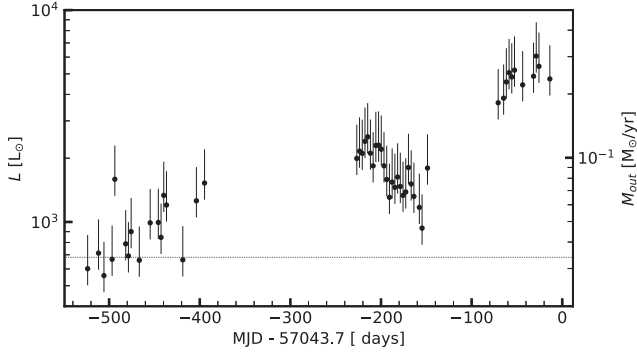
Figure 10. Bolometric luminosity of the precursor emission and mass-loss rate corresponding to an isothermal outflow. The line shows the luminosity of the progenitor.

total luminosity of the system (see Fig. 10). We assume a blackbody emission at the estimated temperature of the progenitor star ($T_{out} = 4300$ K). Scaling the synthetic photometry of the blackbody to the observed flux in the r band allows us to estimate the total bolometric luminosity of the system. We vary T_{out} between 3500 and 8000 K, to illustrate the effect of the temperature uncertainty.

Following Pejcha et al. (2016b), the luminosity of an optically thin outflow powered by the dissipation of energy from shocks within the stream is

$$L_{thin} \sim \frac{1}{2} \dot{M} \Delta v^2, \tag{6}$$

where we adopt $\Delta v / v_{esc} = 0.5/\eta$ with $\eta = 8$. When matched to the observed luminosity, the resulting mass-loss rate is shown in the left-hand axis in Fig. 10. The integrated mass-loss within this period is $M_{out} = 1.4^{+0.6}_{-0.2} \times 10^{-1}$ M$_\odot$.

For an optically thick outflow, not all the energy is radiated, as part goes into the adiabatic expansion of the gas. Numerical results presented in Pejcha et al. (2016b) showed that the maximum asymptotic luminosity of the outflow has a weak dependence on the vertical optical depth of the flow, $\tau_{z,c}$, with

$$L_{thick,max} \sim L_{thin} \max(1, \tau_{z,c})^{-0.2}. \tag{7}$$

Hence, if the temperature of the outflow is maintained constant, we should interpret our mass-loss estimates as lower limits. However, a lower value could still be compatible with the observed luminosity. For example, an increase in the temperature at which matter is ejected from L2 can drive the spiral stream to becomes wider, causing the collisions to occur closer to the binary and increasing the radiative efficiency of the outflow (Pejcha et al. 2016a, 2017). Alternatively, if the outflow is bound to the system, it will form a circumbinary torus (MacLeod et al. 2018b), which can dissipate energy more efficiently than the thin disc approach.

4.2 Late time evolution of the remnant

The luminosity evolution of M31-LRN-2015 at late times (after the termination of the plateau) can be modelled as gravitational contraction of an inflated envelope surrounding the remnant. Similar explanations have been given for the post-outburst luminosity declines observed in V4332 Sgr and V838 Mon. Tylenda et al. (2005) model the photometric evolution assuming gravitational contraction

of an envelope with binding energy

$$E_g = -\frac{GM_* M_e}{(R_* R)^{1/2}}, \tag{8}$$

where M_* is the mass of the remnant, M_e is the mass of the envelope, R_* is the inner radius of the envelope, and R is the outer radius of the envelope. If the luminosity is primarily from gravitational contraction, then

$$L = -\frac{dE_g}{dt} = \frac{GM_* M_e}{2R_*^{1/2}} \frac{1}{R^{3/2}} \frac{dR}{dt}, \tag{9}$$

and since $L = 4\pi R^2 \sigma T_{eff}^4$,

$$\frac{dR}{R^{7/2}} = -\frac{8\pi R_*^{1/2} \sigma T_{eff}^4}{GM_* M_e} dt. \tag{10}$$

For the sake of simplicity, we will assume constant T_{eff} even though our SED analysis shows a possible increase in the temperature. In these phases, our estimate of T_* is strongly influenced by our priors and we consider our approximation acceptable for illustrative purposes. With T_{eff} fixed, equation (10) can be integrated to

$$\frac{1}{R^{5/2}} = \frac{20\pi R_*^{1/2} \sigma T_{eff}^4}{GM_* M_e} t + \frac{1}{R_0^{5/2}}, \tag{11}$$

where R_0 is the envelope radius at the start of the contraction at ($t = 0$). In this simplified model, the late-time luminosity evolution of a gravitationally settling envelope should be $L \propto t^{-4/5}$, which is plotted in the upper panel of Fig. 9. This trend, similar to the one for V838 Mon and V1309 Sco, is observed until 2.5 yr after peak. After that, the object seems to increase in luminosity possibly due to shocks in the ejecta.

4.3 The effect of dust-driven winds

Dust-driven winds are one of the main mechanisms in removing the extended envelopes in asymptotic giant-branch (AGB) stars. The low-temperature and high-density environments generated by stellar pulsations are suitable sites for dust growth. Because of the coupling between dust and gas, the radiation pressure from the star on dust grains provides an efficient way to accelerate the outermost layers to supersonic velocities.

In the case of stellar mergers or successful CE remnants, the envelope has an expanding unbound component, but there is also a significant amount of gas which is still gravitationally bound to the system (Pejcha et al. 2016b; MacLeod et al. 2018b). If this gas is located beyond the dust condensation radius R_C, the dust grains will be able to form and grow. The radiation pressure on the bound gas will eventually accelerate the grains to supersonic speeds and allow gas to escape from the system.

Following Glanz & Perets (2018), we define the dust condensation radius using the properties of the primary star before the start of the CE:

$$R_C = 0.5^{2/5} \left(\frac{T_C}{T_*}\right)^{-2} R_*. \tag{12}$$

Assuming the progenitor parameters (T_*, R_*) derived in Section 3.3, a condensation temperature of $T_C = 1500$ K will be reached at $R_C \simeq 290 R_\odot$. During the outburst, this radius is well within the photosphere of the nova, which is located at $\sim 10^4 R_\odot$, as shown in Fig. 9.

Although a detailed analysis of the dust-driven outflows for M31-LRN-2015 is outside of the scope of this work (see Iaconi et al. 2020 for an analysis of dust formation in CE ejecta),

we would like to highlight that this process may provide the long-sought channel for unbinding large part of the gas from binary systems after the spiral-in and CE ejection had taken place.

5 SUMMARY AND CONCLUSIONS

In this work, we have made an extended observational study of the stellar merger M31-LRN-2015, from 5 yr prior the peak to 5 yr after the peak. The main conclusions of our study are as follows:

(i) The progenitor of M31-LRN-2015 did not have a detectable dust emission component, which sets an upper limit on the dust masses between $10^{-6.4}$ and $10^{-9.7}\,\mathrm{M_\odot}$ for optically thin dust with temperatures of 250 and 1500 K, respectively.

(ii) The system began to brighten 2 yr before peak. At about $\sim -200\,\mathrm{d}$, the light curve dimmed by 1 mag, but the brightening resumed shortly afterwards. This complex luminosity evolution is best explained by the RLOF of the primary and mass-loss from L2 point. Assuming the observed emission is mainly powered by shocks within the self-intersecting stream, the total mass-loss during the precursor phase is $\geq 0.14\,\mathrm{M_\odot}$.

(iii) The light curve of the precursor may show a period of $16.8 \pm 0.3\,\mathrm{d}$ in the dimming phase and $28.1 \pm 1.4\,\mathrm{d}$ in the brightening phase. Although the significance of these period detections is low, we tentatively attribute this periodicity to the characteristics of the outflow from the binary, analogous to the trend observed in V1309 Sco.

(iv) The spectroscopic evolution of the merger initially shows a 5000-K continuum with a superposed forest of narrow absorption lines from low-ionization elements. After the peak, the temperature of the continuum quickly drops, and strong molecular absorption features of TiO and VO appear at $+47\,\mathrm{d}$. By $+140\,\mathrm{d}$, the object has no detectable emission bluewards of 8000 Å and its spectrum resembles a Mira-like M9e-type star.

(v) Before peak, the spectrum shows an Hα emission component centred at the rest-frame velocity. The line temporarily disappears during the plateau phase, and then reappears with a blueshift of $\sim 300\,\mathrm{km\,s^{-1}}$. The redshifted component is likely obscured by dust formed in the eruption.

(vi) During the post-peak light-curve plateau, the SED suggests the existence of an optically thin dust shell located outside the expanding photosphere of the remnant star. For gas at the system's escape velocity, the shell would have been ejected about half a year before the nova event, coinciding with the last brightening episode in the precursor emission.

(vii) After the end of the plateau, the luminosity decreases at a rate consistent with a gravitationally settling giant star. While the merger remnant may become hotter with time, the dust shell cools down from ~ 1700 to $\sim 700\,\mathrm{K}$.

(viii) At late times, the ejecta forms an optically thick ($\tau_V \sim 400$) shell that totally obscures the stellar remnant in optical and NIR wavelengths. The shell has an estimated mass of $M_{\mathrm{ej}} \sim 0.2\,\mathrm{M_\odot}$, in agreement with previous works. Its inner radius is located beyond the dust condensation radius, allowing radiation pressure to further accelerate this dusty matter.

The data and analysis presented in this work shows the importance of late time follow-up for a stellar merger in the IR, revealing the fast dust formation mechanisms, which quickly obscure the nova remnant. Due to its large optical depth, the late-time merger remnant is undetectable in optical and NIR wavelenghts, although still visible in the mid-IR. Some of the SPRITEs (eSPecially Red

Intermediate-luminosity Transient Events) reported by the SPIRITS survey (Kasliwal et al. 2017; Jencson et al. 2019b) show similar characteristics to M31-LRN-2015 at late times, and may also be stellar mergers. The progressive evolution of the object's emission into longer wavelengths makes it an exciting target for the *James Webb Space Telescope* (*JWST*).

is operated by the Jet Propulsion Laboratory, California Institute of Technology, under a contract with NASA. This research made use of ASTROPY,[4] a community-developed core PYTHON package for astronomy (Astropy Collaboration et al. 2013, 2018).

DATA AVAILABILITY

The photometric data and analysis results underlying this study are available in the paper and its online supplementary material. The spectroscopic data underlying this paper are available in the online repository WISEREP (Yaron & Gal-Yam 2012) at https://wiserep.weizmann.ac.il, and can be accessed with the id 'iPTF15t'.

REFERENCES

Adams S. M., Kochanek C. S., 2015, MNRAS, 452, 2195
Adams S., Kochanek C. S., Dong S., Wagner R. M., 2015a, Astron. Telegram, 7468, 1
Adams S., Kochanek C. S., Dong S., Wagner R. M., 2015b, Astron. Telegram, 7485, 1
Adams S. M., Kochanek C. S., Prieto J. L., Dai X., Shappee B. J., Stanek K. Z., 2016, MNRAS, 460, 1645
Adams S. M., Kochanek C. S., Gerke J. R., Stanek K. Z., Dai X., 2017, MNRAS, 468, 4968
Adams S. M. et al., 2018, PASP, 130, 034202
Astropy Collaboration et al., 2013, A&A, 558, A33
Astropy Collaboration et al., 2018, AJ, 156, 123
Bersier D., Kochanek C. S., Wagner R. M., Adams S., Dong S., 2015, Astron. Telegram, 7537, 1
Bildsten L., Shen K. J., Weinberg N. N., Nelemans G., 2007, ApJ, 662, L95
Blagorodnova N. et al., 2017, ApJ, 834, 107
Bond H. E., Bedin L. R., Bonanos A. Z., Humphreys R. M., Monard L. A. G. B., Prieto J. L., Walter F. M., 2009, ApJ, 695, L154
Botticella M. T. et al., 2009, MNRAS, 398, 1041
Chambers K. C. et al., 2016, preprint (arXiv:1612.05560)
Chemin L., Carignan C., Foster T., 2009, ApJ, 705, 1395
Darwin G. H., 1879, Proc. R. Soc. I, 29, 168
Dominik M., Belczynski K., Fryer C., Holz D. E., Berti E., Bulik T., Mandel I., O'Shaughnessy R., 2012, ApJ, 759, 52
Dong S., Kochanek C. S., Adams S., Prieto J.-L., 2015, Astron. Telegram, 7173, 1
Draine B. T., Lee H. M., 1984, ApJ, 285, 89
Draine B. T. et al., 2014, ApJ, 780, 172
Elitzur M., Ivezić Ž., 2001, MNRAS, 327, 403
Fabrika S. et al., 2015, Astron. Telegram, 6985, 1
Fazio G. G. et al., 2004, ApJS, 154, 10
Freedman W. L., Madore B. F., 1990, ApJ, 365, 186
Gehrz R. D. et al., 2007, Rev. Sci. Instrum., 78, 011302
Geier S., Pessev P., 2015, Astron. Telegram, 8220, 1
Giallongo E. et al., 2008, A&A, 482, 349
Glanz H., Perets H. B., 2018, MNRAS, 478, L12
Gunn J. E., Stryker L. L., 1983, ApJS, 52, 121
Harmanen J., McCollum B., Laine S., Rottler L., Bruhweiler F. C., 2015, Astron. Telegram, 7595, 1
Hill J. M., Green R. F., Slagle J. H., 2006, in Stepp L. M., ed., Proc. SPIE Conf. Ser. Vol. 6267, Ground-based and Airborne Telescopes. SPIE, Bellingham, p. 62670Y
Hodgkin S. T. et al., 2015, Astron. Telegram, 6952, 1
Howitt G., Stevenson S., Vigna-Gómez A., Justham S., Ivanova N., Woods T. E., Neijssel C. J., Mandel I., 2020, MNRAS, 492, 3229
Iaconi R., Maeda K., Nozawa T., De Marco O., Reichardt T., 2020, preprint (arXiv:2003.06151)
Ivanova N. et al., 2013a, A&A Rev., 21, 59

Ivanova N., Justham S., Avendano Nandez J. L., Lombardi J. C., 2013b, Science, 339, 433
Ivezic Z., Elitzur M., 1997, MNRAS, 287, 799
Ivezic Z., Nenkova M., Elitzur M., 1999, preprint (astro-ph/9910475)
Izzard R. G., Hall P. D., Tauris T. M., Tout C. A., 2012, in Manchado A., Stanghellini L., Schönberner D., eds, Proc. IAU Symp. 283, Planetary Nebulae: An Eye to the Future. p. 95
Jacoby G. H., Hunter D. A., Christian C. A., 1984, ApJS, 56, 257
Jencson J. E. et al., 2019a, ApJ, 880, L20
Jencson J. E. et al., 2019b, ApJ, 886, 40
Kamiński T., Tylenda R., 2011, A&A, 527, A75
Kamiński T., Mason E., Tylenda R., Schmidt M. R., 2015, A&A, 580, A34
Kamiński T. et al., 2017, A&A, 599, A59
Kasliwal M. M., 2012, Publ. Astron. Soc. Aust., 29, 482
Kasliwal M. M. et al., 2012, ApJ, 755, 161
Kasliwal M. M. et al., 2017, ApJ, 839, 88
Keenan P. C., Garrison R. F., Deutsch A. J., 1974, ApJS, 28, 271
Klencki J., Nelemans G., Istrate A. G., Chruslinska M., 2020, preprint (arXiv:2006.11286)
Kochanek C. S., Adams S. M., Belczynski K., 2014, MNRAS, 443, 1319
Kulkarni S. R., 2013, Astron. Telegram, 4807, 1
Kulkarni S. R. et al., 2007, Nature, 447, 458
Kurtenkov A. A. et al., 2015a, A&A, 578, L10
Kurtenkov A., Ovcharov E., Nedialkov P., Kostov A., Bachev R., Dimitrova R. V. M., Popov V., Valcheva A., 2015b, Astron. Telegram, 6941, 1
Laor A., Draine B. T., 1993, ApJ, 402, 441
Law N. M. et al., 2009, PASP, 121, 1395
Law N. M. et al., 2010, in McLean I. S., Ramsay S. K., Takami H., eds, Proc. SPIE Conf. Ser. Vol. 7735, Ground-based and Airborne Instrumentation for Astronomy III. SPIE, Bellingham, p. 77353M
Lipunov V. M. et al., 2017, MNRAS, 470, 2339
Lodders K., 2003, ApJ, 591, 1220
Lomb N. R., 1976, Ap&SS, 39, 447
Lopez-Camara D., Moreno Mendez E., De Colle F., 2020, MNRAS, preprint (arXiv:2004.04158)
Lü G., Zhu C., Podsiadlowski P., 2013, ApJ, 768, 193
MacLeod M., Loeb A., 2020, ApJ, 895, 29
MacLeod M., Macias P., Ramirez-Ruiz E., Grindlay J., Batta A., Montes G., 2017, ApJ, 835, 282
MacLeod M., Ostriker E. C., Stone J. M., 2018a, ApJ, 863, 5
MacLeod M., Ostriker E. C., Stone J. M., 2018b, ApJ, 868, 136
Martini P., Wagner R. M., Tomaney A., Rich R. M., della Valle M., Hauschildt P. H., 1999, AJ, 118, 1034
Masci F. J. et al., 2017, PASP, 129, 014002
Mason E., Diaz M., Williams R. E., Preston G., Bensby T., 2010, A&A, 516, A108
Mathis J. S., Rumpl W., Nordsieck K. H., 1977, ApJ, 217, 425
Mauerhan J. C., Van Dyk S. D., Johansson J., Fox O. D., Filippenko A. V., Graham M. L., 2018, MNRAS, 473, 3765
Metzger B. D., Pejcha O., 2017, MNRAS, 471, 3200
Montalto M., Seitz S., Riffeser A., Hopp U., Lee C.-H., Schönrich R., 2009, A&A, 507, 283
Moreno Méndez E., López-Cámara D., De Colle F., 2017, MNRAS, 470, 2929
Mould J. et al., 1990, ApJ, 353, L35
Munari U. et al., 2002, A&A, 389, L51
Oke J. B. et al., 1995, PASP, 107, 375
Ossenkopf V., Henning T., 1994, A&A, 291, 943
Ovcharov E., Kurtenkov A., Valcheva A., Nedialkov P., 2015, Astron. Telegram, 6924, 1
Paczynski B., 1976, in Eggleton P., Mitton S., Whelan J., eds, Proc. IAU Symp. 73, Structure and Evolution of Close Binary Systems. Kluwer, Dordrecht, p. 75
Pastorello A., Fraser M., 2019, Nat. Astron., 3, 676
Pastorello A. et al., 2019a, A&A, 625, L8
Pastorello A. et al., 2019b, A&A, 630, A75
Pejcha O., 2014, ApJ, 788, 22
Pejcha O., Metzger B. D., Tomida K., 2016a, MNRAS, 461, 2527

----

[4] http://www.astropy.org.

Pejcha O., Metzger B. D., Tomida K., 2016b, MNRAS, 455, 4351

Pejcha O., Metzger B. D., Tyles J. G., Tomida K., 2017, ApJ, 850, 59

Pessev P., Geier S., Kurtenkov A., Nielsen L. D., Tomov T., 2015a, Astron. Telegram, 7272, 1

Pessev P., Geier S., Kurtenkov A., Nielsen L. D., Slumstrup D., Tomov T., 2015b, Astron. Telegram, 7572, 1

Pessev P., Geier S., Stritzinger M., Kurtenkov A., Tomov T., 2015c, Astron. Telegram, 7624, 1

Pessev P., Geier S., Stritzinger M., Kurtenkov A., Tomov T., 2015d, Astron. Telegram, 8059, 1

Prieto J. L., Sellgren K., Thompson T. A., Kochanek C. S., 2009, ApJ, 705, 1425

Rahmer G., Smith R., Velur V., Hale D., Law N., Bui K., Petrie H., Dekany R., 2008, in McLean I. S., Casali M. M., eds, Proc. SPIE Conf. Ser. Vol. 7014, Ground-based and Airborne Instrumentation for Astronomy II. SPIE, Bellingham, p. 70144Y

Rasio F. A., 1995, ApJ, 444, L41

Rau A. et al., 2009, PASP, 121, 1334

Reichardt T. A., De Marco O., Iaconi R., Tout C. A., Price D. J., 2019, MNRAS, 484, 631

Rich R. M., Mould J., Picard A., Frogel J. A., Davies R., 1989, ApJ, 341, L51

Scargle J. D., 1982, ApJ, 263, 835

Schlafly E. F. et al., 2012, ApJ, 756, 158

Schlegel D. J., Finkbeiner D. P., Davis M., 1998, ApJ, 500, 525

Seifert W. et al., 2003, in Iye M., Moorwood A. F. M., eds, Proc. SPIE Conf. Ser. Vol. 4841, Instrument Design and Performance for Optical/Infrared Ground-based Telescopes. SPIE, Bellingham, p. 962

Shiber S., Soker N., 2018, MNRAS, 477, 2584

Shiber S., Iaconi R., De Marco O., Soker N., 2019, MNRAS, 488, 5615

Shumkov V. et al., 2015a, Astron. Telegram, 6911, 1

Shumkov V. et al., 2015b, Astron. Telegram, 6951, 1

Smith N., Li W., Silverman J. M., Ganeshalingam M., Filippenko A. V., 2011, MNRAS, 415, 773

Smith N. et al., 2016, MNRAS, 458, 950

Srivastava M., Ashok N. M., Banerjee D. P. K., Venkataraman V., 2015, Astron. Telegram, 7236, 1

Steele I. A., Williams S. C., Darnley M. J., Bode M. F., Barnsley R. M., Smith R. J., Jermak H. E., 2015, Astron. Telegram, 7555, 1

Thompson T. A., Prieto J. L., Stanek K. Z., Kistler M. D., Beacom J. F., Kochanek C. S., 2009, ApJ, 705, 1364

Tylenda R., 2005, A&A, 436, 1009

Tylenda R., Kamiński T., 2016, A&A, 592, A134

Tylenda R., Crause L. A., Górny S. K., Schmidt M. R., 2005, A&A, 439, 651

Tylenda R. et al., 2011, A&A, 528, A114

Tylenda R. et al., 2013, A&A, 555, A16

Vigna-Gómez A., MacLeod M., Neijssel C. J., Broekgaarden F. S., Justham S., Howitt G., de Mink S. E., Mandel I., 2020, preprint (arXiv:2001.09829)

Wagner R. M., Starrfield S. G., Wilber A., Kochanek C. S., Dong S., Prieto J.-L., Adams S., 2015, Astron. Telegram, 7208, 1

Werner M. W. et al., 2004, ApJS, 154, 1

Williams S. C., Darnley M. J., Bode M. F., Steele I. A., 2015, ApJ, 805, L18

Wizinowich P. L. et al., 2006, PASP, 118, 297

Wozniak P. R., 2000, Acta Astron., 50, 421

Yaron O., Gal-Yam A., 2012, PASP, 124, 668

SUPPORTING INFORMATION

Supplementary data are available at *MNRAS* online.

Figure 2. PTF/iPTF light curve of M31-LRN-2015 in Mould-*R* (red) and *g* bands (green).

Figure 3. Light curve showing PTF/iPTF photometry, along with our NIR and MIR data.

Please note: Oxford University Press is not responsible for the content or functionality of any supporting materials supplied by the authors. Any queries (other than missing material) should be directed to the corresponding author for the article.

This paper has been typeset from a TeX/LaTeX file prepared by the author.